Biomechanics and Modeling in Mechanobiology
https://doi.org/10.1007/s10237-022-01595-0

ORIGINAL PAPER

Anisotropy profoundly alters stress fields within contractile cells and cell aggregates

Habibeh Ashouri Choshali[1] · **Kristen L. Billiar**[2] · **Nima Rahbar**[1]

Received: 23 October 2021 / Accepted: 12 May 2022

Abstract

Many biological phenomena such as cell proliferation and death are correlated with stress fields within cells. Stress fields are quantified using computational methods which rely on fundamental assumptions about local mechanical properties. Most existing methods such as Monolayer Stress Microscopy assume isotropic properties, yet experimental observations strongly suggest anisotropy. We first model anisotropy in circular cells analytically using Eshelby's inclusion method. Our solution reveals that uniform anisotropy cannot exist in cells due to the occurrence of substantial stress concentration in the central region. A more realistic non-uniform anisotropy model is then introduced based on experimental observations and implemented numerically which interestingly clears out stress concentration. Stresses within the entire aggregate also drastically change compared to the isotropic case, resulting in better agreement with observed biomarkers. We provide a physics-based mechanism to explain the low alignment of stress fibers in the center of cells, which might explain certain biological phenomena e.g., existence of disrupted rounded cells, and higher apoptosis rate at the center of circular aggregates.

Keywords Anisotropic contractility · Circular constrained cells · Mechanical stress · Stress-biomarker relations

1 Introduction

Mechanical factors (e.g., force, stress, and strain) generated within living cells as a result of actomyosin machinery activity have been found to act as key regulators of the cell behavior. Cell fate (Liu et al. 2016; Cabezas et al. 2019; Discher et al. 2009; Vogel and Sheetz 2006), transcriptional regulators TAZ and YAP (Aragona 2013; Dupont 2011), cell proliferation and differentiation (Nelson 2005; Li et al. 2009; Wan 2010), cell polarization and alignment (He 2015), and cell migration (Ng et al. 2012; Lo et al. 2000), all have been shown to correlate with mechanical factors. These phenomena play a crucial role in morphogenesis, wound healing, and tumour metastasis (Trepat 2009; Olson and Sahai 2009).

Quantifying the mechanical factors helps understand the relationship between stress and cell behavior. The stress field in living cells cannot be experimentally measured and can only be calculated using computational or theoretical methods. For colonies with highly motile cells, non-continuum mechanics models such as Cellular Potts model (Graner and Glazier 1992; Albert and Schwarz 2014) and vertex model (Honda and Eguchi 1980; Farhadifar et al. 2007; Schaumann et al. 2018), have been widely used. However, for single cells and confluent and/or strongly adherent multicellular aggregates that are not highly motile, continuum models have been able to well describe the mechanical response of the system (Hur et al. 2009; Nelson 2005). A continuum model typically considers the single cell or multicellular aggregate as a continuous medium under a contraction caused by actomyosin contractility (Schaumann et al. 2018). Traction force microscopy is a widely used technique that uses the continuum model to quantify stress/strain fields in biological cells (Hazeltine 2012; Huang 2019). In traction force microscopy, the deformation field is experimentally measured and then the stress field in the cell layer is calculated using a computational approach. Li et al. considered aggregated cell islands as a homogeneous isotropic continuum medium and modelled the contractility using a

---

✉ Nima Rahbar
nrahbar@wpi.edu

[1] Department of Civil and Environmental Engineering, Worcester Polytechnic Institute, 100 Institute Rd, Worcester, MA 01609, USA

[2] Department of Biomedical Engineering, Worcester Polytechnic Institute, 100 Institute Rd, Worcester, MA 01609, USA

temperature drop to obtain mechanical stress patterns (Li et al. 2009). They found that certain levels of mechanical stress affect cell proliferation and differentiation patterns. He et al. considered the cell layer as a continuum homogeneous elastic membrane and observed that the in-plane maximum shear stress in the cell layer directs the arrangement and polarization of cells (He 2015). Tambe et al. considered a monolayer consisting of multiple contiguous cells as a thin flat sheet and developed the governing equations for monolayer stress microscopy (Tambe 2013).

Previous continuum models have assumed simplifying assumptions for material properties of the cell layer (Hur et al. 2009; Nelson 2005; Li et al. 2009; He 2015; Tambe 2013, 2011). One of these simplifications is homogeneity, whereas many experimental studies have observed heterogeneity in the cell layer properties. For example, modulus, average spread area, and traction force of the cell all have been shown to vary along the radius of the circular multicellular aggregates (Goldblatt 2020). On the other hand, it has been found that mechanical-induced biological activities vary by region within the multi-cellular aggregates. For example, investigation of the activity of Caspase 3/7 has shown accumulation of programmed cell death (apoptosis) within the central region of circular aggregates (Cirka 2016; Goldblatt 2020) (Fig. 1). Also, proliferation, polarization, and alignment of cells are shown to be less at the center of circular aggregates (Nelson 2005; He 2015). We have shown that heterogeneous properties of cell layer can invert the trend of stress field within the cell monolayer when compared to the trend in the case of homogeneous properties (Goldblatt 2020). The inverted trend (i.e., low average stress in central regions and high average stress at the periphery of the aggregates) was found to be more consistent with biological bio-markers (Goldblatt 2020).

Another simplification in previous continuum models is isotropy. Anisotropy has been widely observed in biological tissues (Feng et al. 2017; Braeu et al. 2019). In tissues such as blood vessels and tendons, the stiffness in different directions at the same point can be different by as large as two orders of magnitude (Wilson et al. 2013; Yin and Elliott 2004). More importantly, anisotropy has been widely observed in living cells (Crouch et al. 2009; Hu 2003), the building blocks of tissues. Indentation experiments by Efremov et al. showed strong anisotropy in cells with perinuclear actin cap, while cells with disrupted or no actin cap, like cancerous cells, showed an isotropic behavior (Efremov 2019). They then quantified the measured mechanical properties and showed that for cell types with anisotropic

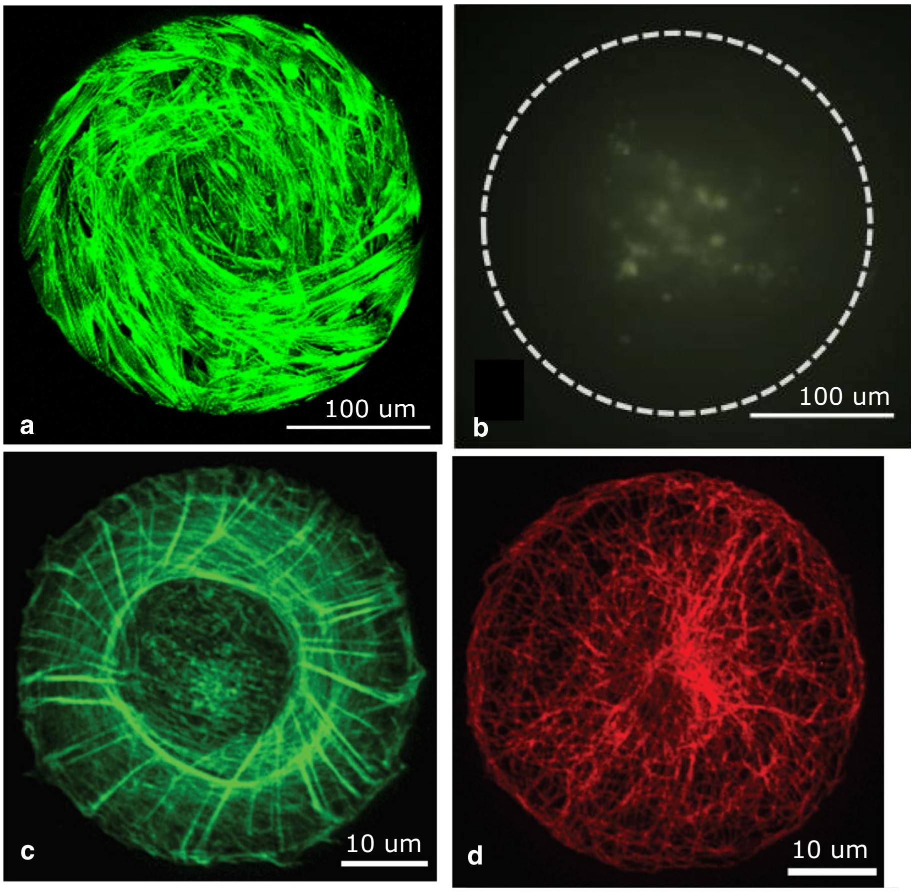

Fig. 1 **a** Reprinted from (Cirka 2016): F-actin alignment increases from the center to edge of the aggregate. **b** Reprinted from (Cirka 2016): The activity of Caspase 3/7 [which is an indicator of programmed cell death (Grütter 2000)] dominates within central region of aggregates. **c**, **d** Reprinted from (Tee 2015): Organization of the actin cytoskeleton system; **c** showing a combined radial/circumferential alignment; and **d** showing a microtubule system with higher intensity at the center

behavior, the modulus in the direction of fiber alignment can be several orders of magnitude larger than the effective isotropic modulus, while the modulus in both directions perpendicular to the fiber alignment can be about fifty percent smaller than the effective isotropic modulus. It is believed that this strong anisotropy in living cells occurs due to the presence and alignment of stress fibers such as F-actin (Peeters 2004; Hu 2004; Gupta et al. 2019; Crouch et al. 2009; Fouchard et al. 2011). F-actin fibers are tensional load carrying elements and their alignment increases the local contractility and stiffness in the direction of alignment (Smith et al. 2003; Efremov 2019). For a multi-cellular aggregate cultured on a circular shape (Fig. 1a), the circumferential fiber alignment is the dominant pattern, with a non-uniform intensity where the alignment increases from center to edge along the radius (Cirka 2016). We have previously shown that the F-actin alignment index, determined by processing phalloidin-stained actin images, increases from the center to the edge of the aggregate [Fig. 2d of Ref. (Goldblatt 2020)]. In an independent study, He et al. showed that the cell polarization and alignment are highest at the edge of disk/ring patterns, promoting higher contractility in the alignment (radial) direction [Fig. 2 of Ref. (He 2015)]. For a single cell cultured on a circular shape (Fig. 1c), radial and circumferential F-actin alignments are dominant patterns, again with a non-uniform intensity where there is almost no alignment at the center but very intense alignment at the edge (Tee 2015; Cabezas et al. 2019; Gupta 2015).

In this paper, we hypothesize that anisotropy substantially alters emergent stress fields within circular constrained aggregates and cells by using a continuum-based combined theoretical and computational approach. For the sake of simplicity, hereafter we use the term “cell layer” to refer to both circular aggregate and single cell, unless specifically mentioned. We first use the Eshelby’s inclusion method to obtain a closed-form solution for the stress field within a cell layer with general properties. To this end, we model the effect of anisotropic contractility on the elastic fields by an appropriate eigenstrain field applied to the inclusion problem equivalent to the cell layer. It is worth mentioning that the force induced by the substrate acts as traction stresses (boundary conditions) on the cell layer. Subsequently elastic fields of three problems with free boundary conditions are analytically solved: (i) a multicellular cell layer with actin fibers dominantly aligned along the circumference; (ii) a single cell layer with actin fibers dominantly aligned along the radius; and (iii) a single cell layer with actin fibers dominantly aligned along the circumference. The case of free boundary condition is more for the purpose of validating the numerical solution. While this boundary condition is hypothetical, our study shows that this case provides a basis solution for more realistic boundary conditions. We then build a thermal-contraction finite-element model to later study more complex anisotropy models and boundary conditions, (e.g., cell layer attached to the substrate), for which analytical solution becomes troublesome. Even though we use the concept of thermal contraction, the biological response of cells under temperature change is not the focus of this study. In this work, the contractility in the cell layer is simulated by a thermal contraction proportional to the thermal expansion coefficient (He 2015; Nelson 2005). We validate the finite-element model by comparing the computational and analytical results for all three problems mentioned above. Both analytical and computational results, in good agreement, show that stress singularity occurs at the center of the cell layer for the uniform anisotropy model. Stress singularity is a theoretical/mathematical concept in the context of elasticity theory, which means that stresses approach infinity. However, in the realistic case, the singularity shows itself as stress concentration. Finally, we suggest an experimentally-based non-uniform anisotropic contractility model (zero anisotropy at the center and maximum anisotropy at periphery) for a multicellular cell layer. We then extend the analytical results using the thermal-contraction finite-element model for the more realistic anisotropy model and boundary conditions.

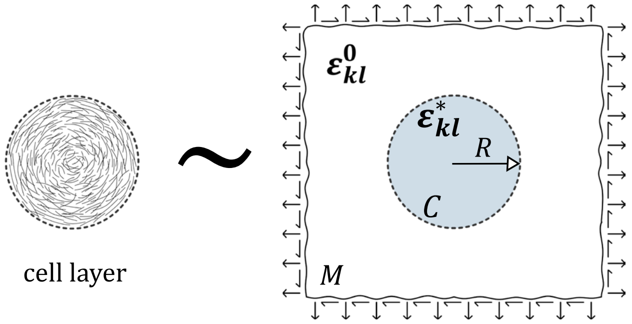

Fig. 2 A schematic showing that a cell layer (on the left) having a cylindrical anisotropy is replaced with an equivalent Eshelby’s inclusion (on the right) having uniform isotropic properties, under an appropriately selected eigenstrain field and far-field strain

2 Materials and methods

2.1 Analytical model

Circularly shaped aggregates that are cultured to confluence or post-confluence levels, as well as circularly shaped single cells, can be considered as a continuous thin cylindrical layer (Nelson 2005; Li et al. 2009; He 2015). The elasticity problem for an anisotropic cylindrical body has been formulated by previous researchers; in general, these formulations result in tedious algebra, therefore the implications have been limited to certain symmetry and loading types (Ting 1996; Oral and Anlas 2005). Cylindrical anisotropy refers to the case where the material property tensor has one axis of symmetry among cylindrical coordinates (r, θ, z) (Allen and Farris 1990). The special case of cylindrical anisotropy with z being the axis of symmetry is relatively simpler and has been widely studied for different applications (Lu et al. 2016). In the problem of interest in this paper though, we are dealing with either r or θ being the axis of symmetry: For circularly shaped multi-cellular aggregates and single cells, either circumferential or radial alignment of F-actin fibers are commonly observed (Tee 2015; Cabezas et al. 2019; Goldblatt 2020; Cirka 2016); both circumferential and radial types of cylindrical anisotropy create coupling between radial and circumferential elastic fields, and therefore lead to cumbersome formulations (Allen and Farris 1990). Circumferential F-actin alignment causes higher circumferential contractility compared to radial and axial (z) directions (Fig. 1a), whereas radial F-actin alignment causes higher radial contractility compared to circumferential and axial directions (Fig. 1c).

Eshelby's inclusion method formulation can reduce the complexity of elasticity equations of a general cylindrical anisotropic body. This method was originally employed in micromechanics of defects (Mura 2013). However, it is based on a continuum theory of elasticity with applications in many areas related to the mechanical behavior of materials such as composites. This approach can be used to analyze a wide range of mechanical problems by using the concept of "eigenstrain". In the context of Eshelby's inclusion method, eigenstrain is a general name given to any non-direct elastic strain such as thermal strain, misfit strain, and pre-strain. Also, an inclusion by definition is a subdomain C inside domain $M \cup C$ where the elastic moduli of C are the same as those of M, Fig. 2. The eigenstrain $\boldsymbol{\epsilon}^*$ is zero in M and is nonzero in C in general (Mura et al. 1996). Since in reality, cells are surrounded by fluids that exert negligible traction forces to the cell layer periphery, (due to the lack of the presence of side focal adhesions), in our analytical model for the cell layer, we adjust the boundary conditions in a way that the traction components at the boundary become zero, as if the domain M does not exist.

Cells generate mechanical forces which arise from actomyosin contraction (Ingber 1991; Fouchard et al. 2011). This contraction can be modeled by a pre-strain, i.e., an eigenstrain (Nelson 2005; He 2015). The main idea here is to replace the cell layer having a general cylindrical anisotropy with an equivalent Eshelby's inclusion which is an elastic medium, under a proper choice of eigenstrain, $\boldsymbol{\epsilon}^*$ defined over the region C, and far-field strain, Fig. 2. We should clarify that the infinite medium around the inclusion is a conceptual medium and is different from the real substrate that the cell is attached to, but we can use this concept to use the Eshelby's inclusion method formulation. We will choose the far-field strain of the infinite medium such that the boundary conditions at the edge of the cell are satisfied as desired.

We begin with reformulating the equations of linear elasticity in the cylindrical coordinate system. Troublesome partial differential equations can be simplified to solvable ordinary differential equations by expansion in terms of an orthogonal cylindrical basis. The stress, strain, and displacement fields can be expanded as follows:

$$\mathbf{u}(r,\theta,z) = \sum_{i=r,\theta,z} \sum_{\eta,\xi} u_i^{(\eta,\xi)}(r)\, e^{\imath\eta\theta} e^{\imath\xi\pi z}\, \mathbf{e}_i\,, \tag{1a}$$

$$\begin{aligned}&\left\{\boldsymbol{\epsilon}(r,\theta,z), \boldsymbol{\epsilon}^*(r,\theta,z), \boldsymbol{\sigma}(r,\theta,z)\right\}\\ &\quad= \sum_{i,j=r,\theta,z} \sum_{\eta,\xi} \{\epsilon_{ij}^{(\eta,\xi)}(r), \epsilon_{ij}^{*(\eta,\xi)}(r), \sigma_{ij}^{(\eta,\xi)}(r)\}\, e^{\imath\eta\theta} e^{\imath\xi\pi z}\, \mathbf{e}_i\, \mathbf{e}_j\,,\end{aligned} \tag{1b}$$

where $\imath$ is the imaginary unit, and for each integer-pair $(\eta,\ \xi)$ in the Fourier series expansion, the expansion coefficients $u_i^{(\eta,\xi)}(r)$, $\epsilon_{ij}^{(\eta,\xi)}(r)$, and $\sigma_{ij}^{(\eta,\xi)}(r)$ are functions of r only.

In order to find an analytical solution, we make the following simplifying assumptions: (i) We consider a thin cell layer, (i.e., the radius of the cell layer is considerably larger than the thickness of the cell layer). (ii) we ignore the tractions applied by the substrate. This is equivalent to the case where cells are not attached to the substrate below them. While this is a simplified hypothetical boundary condition, it still serves as a basis solution for more realistic boundary conditions. We will later numerically study the effect of substrate tractions (i.e., the case where cells are attached to the substrate below them). Using these assumptions, we can neglect the variations along the thickness, i.e., $\xi = 0$. So the expansions will be simplified to

$$\mathbf{u}(r,\theta) = \sum_{i=r,\theta} \sum_{\eta} u_i^{\eta}(r)\, e^{\imath\eta\theta}\, \mathbf{e}_i\,, \tag{2a}$$

$$\begin{aligned}&\left\{\boldsymbol{\epsilon}(r,\theta), \boldsymbol{\epsilon}^*(r,\theta), \boldsymbol{\sigma}(r,\theta)\right\}\\ &\quad= \sum_{i,j=r,\theta} \sum_{\eta} \left\{\epsilon_{ij}^{\eta}(r), \epsilon_{ij}^{*\eta}(r), \sigma_{ij}^{\eta}(r)\right\} e^{\imath\eta\theta}\, \mathbf{e}_i\, \mathbf{e}_j\,.\end{aligned} \tag{2b}$$

2.1.1 Strain-displacement relations

Assuming that the cells are not highly motile, small-strain theory of elasticity, $\boldsymbol{\epsilon} = \frac{1}{2}\left\{\boldsymbol{\nabla}\mathbf{u} + (\boldsymbol{\nabla}\mathbf{u})^T\right\}$ (Sadd 2009), where $\boldsymbol{\nabla}$ is the gradient operator, can be used to express the strain-displacement relation (He 2015). This assumption has been widely used in previous studies to model the mechanical behavior of living cells (e.g., Tambe et al. used small strain theory to analytically investigate Monolayer Stress

Microscopy (Tambe 2013). In another study, He et al. used small strain theory to quantitatively study the cell layer stress field (He 2015)). Using the formulation in cylindrical coordinate system and then by expanding **u** and $\boldsymbol{\epsilon}$ based on Eq. 2a and Eq. 2b, the following strain-displacement relations are obtained in the cylindrical coordinate system:

$$
\begin{aligned}
&\epsilon^{\eta}_{rr}(r) = \frac{du^{\eta}_{r}(r)}{dr}\,,\\
&\epsilon^{\eta}_{\theta\theta}(r) = \frac{u^{\eta}_{r}(r)}{r} + \iota\eta\frac{u^{\eta}_{\theta}(r)}{r}\,,\\
&\epsilon^{\eta}_{zz}(r) = 0,\\
&\epsilon^{\eta}_{r\theta}(r) = \frac{\iota\eta}{2}\frac{u^{\eta}_{r}(r)}{r} - \frac{1}{2}\frac{u^{\eta}_{\theta}(r)}{r} + \frac{1}{2}\frac{du^{\eta}_{\theta}(r)}{dr}\,,\\
&\epsilon^{\eta}_{rz}(r) = \frac{1}{2}\frac{du^{\eta}_{z}(r)}{dr}\,,\\
&\epsilon^{\eta}_{\theta z}(r) = \frac{\iota\eta}{2}\frac{u^{\eta}_{z}(r)}{r}\,.
\end{aligned}
\tag{3}
$$

2.1.2 Stress–strain relations

The linear elastic model, which is a simplification of viscoelastic model, has been widely used to theoretically express the stress-strain relations in living cells (Wei 2020; He 2015; Tambe 2013). Although the time factor will be neglected, the linear elastic solution provides a basis for viscoelastic solution according to the correspondence principle (Hemp 1966; Lim et al. 2006). A linear elastic transversely isotropic material has five independent elastic constants (Sadd 2009). In the general case when the material is also radially heterogeneous from the origin, the stress-strain relations for the transversely isotropic material considered here can be written as

$$
\begin{aligned}
&\sigma_{rr} = C_{11}(r)\,\epsilon_{rr} + C_{12}(r)\,\epsilon_{\theta\theta} + C_{13}(r)\,\epsilon_{zz}\,,\\
&\quad\sigma_{r\theta} = 2\,C_{44}(r)\,\epsilon_{r\theta}\,,\\
&\sigma_{\theta\theta} = C_{12}(r)\,\epsilon_{rr} + C_{22}(r)\,\epsilon_{\theta\theta} + C_{12}(r)\,\epsilon_{zz}\,,\\
&\quad\sigma_{rz} = \big(C_{11}(r) - C_{12}(r)\big)\,\epsilon_{rz}\,,\\
&\sigma_{zz} = C_{13}(r)\,\epsilon_{rr} + C_{12}(r)\,\epsilon_{\theta\theta} + C_{11}(r)\,\epsilon_{zz}\,,\\
&\quad\sigma_{\theta z} = 2\,C_{44}(r)\,\epsilon_{\theta z}\,.
\end{aligned}
\tag{4}
$$

Expanding $\boldsymbol{\epsilon}(r,\theta)$ and $\boldsymbol{\sigma}(r,\theta)$ as in Eq. 2b, stress-strain relations can be re-written in terms of stress and strain coefficient functions as

$$
\begin{aligned}
&\sigma^{\eta}_{rr}(r) = C_{11}(r)\,\epsilon^{\eta}_{rr}(r) + C_{12}(r)\,\epsilon^{\eta}_{\theta\theta}(r) + C_{13}(r)\,\epsilon^{\eta}_{zz}(r)\,,\\
&\sigma^{\eta}_{\theta\theta}(r) = C_{12}(r)\,\epsilon^{\eta}_{rr}(r) + C_{22}(r)\,\epsilon^{\eta}_{\theta\theta}(r) + C_{12}(r)\,\epsilon^{\eta}_{zz}(r)\,,\\
&\sigma^{\eta}_{zz}(r) = C_{13}(r)\,\epsilon^{\eta}_{rr}(r) + C_{12}(r)\,\epsilon^{\eta}_{\theta\theta}(r) + C_{11}(r)\,\epsilon^{\eta}_{zz}(r)\,,\\
&\sigma^{\eta}_{r\theta}(r) = 2\,C_{44}(r)\,\epsilon^{\eta}_{r\theta}(r)\,,\\
&\sigma^{\eta}_{rz}(r) = \big(C_{11}(r) - C_{12}(r)\big)\,\epsilon^{\eta}_{rz}(r)\,,\\
&\sigma^{\eta}_{\theta z}(r) = 2\,C_{44}(r)\,\epsilon^{\eta}_{\theta z}(r)\,.
\end{aligned}
\tag{5}
$$

For an isotropic homogeneous material, the stress-strain relations can be further simplified as

$$
\begin{aligned}
&\sigma^{\eta}_{rr}(r) = (2\mu + \lambda)\,\epsilon^{\eta}_{rr}(r) + \lambda\,\epsilon^{\eta}_{\theta\theta}(r) + \lambda\,\epsilon^{\eta}_{zz}(r)\,,\\
&\sigma^{\eta}_{\theta\theta}(r) = \lambda\,\epsilon^{\eta}_{rr}(r) + (2\mu + \lambda)\,\epsilon^{\eta}_{\theta\theta}(r) + \lambda\,\epsilon^{\eta}_{zz}(r)\,,\\
&\sigma^{\eta}_{zz}(r) = \lambda\,\epsilon^{\eta}_{rr}(r) + \lambda\,\epsilon^{\eta}_{\theta\theta}(r) + (2\mu + \lambda)\,\epsilon^{\eta}_{zz}(r)\,,\\
&\sigma^{\eta}_{r\theta}(r) = 2\mu\,\epsilon^{\eta}_{r\theta}(r)\,,\\
&\sigma^{\eta}_{rz}(r) = 2\mu\,\epsilon^{\eta}_{rz}(r)\,,\\
&\sigma^{\eta}_{\theta z}(r) = 2\mu\,\epsilon^{\eta}_{\theta z}(r)\,,
\end{aligned}
\tag{6}
$$

in which μ is the shear modulus and λ is the Lame's constant which is equal to $2\mu\nu/(1-2\nu)$ where ν is the Poisson's ratio.

2.1.3 Inclusion problem

Let us consider a cylindrical inclusion inside an infinite medium under a given eigenstrain $\boldsymbol{\epsilon}^{*}$ defined over the region C (right side of Fig. 2). The eigenstrain will cause a disturbance strain field, $\boldsymbol{\epsilon}^{\mathrm{d}}$, both inside and outside of the inclusion (Eshelby 1957; Yu et al. 1994; Shodja et al. 2003):

$$
\boldsymbol{\epsilon}^{\mathrm{d}} = \mathbf{D}\boldsymbol{\epsilon}^{*},
\tag{7}
$$

where $\mathbf{D}$ is the Eshelby tensor and $\boldsymbol{\epsilon}^{*}$ is the eigenstrain. Eq. 7 is valid for all points both inside ($\boldsymbol{\epsilon}^{\mathrm{d}(C)} = \mathbf{D}^{C}\boldsymbol{\epsilon}^{*}$) and outside ($\boldsymbol{\epsilon}^{\mathrm{d}(M)} = \mathbf{D}^{M}\boldsymbol{\epsilon}^{*}$) the inclusion. Eshelby tensor for inside the inclusion ($\mathbf{D}^{C}$) is generally different from that outside the inclusion in the matrix ($\mathbf{D}^{M}$). It has been shown that components of the Eshelby tensor in the Cartesian coordinate system are constant, whereas, in the cylindrical coordinate system, components of the Eshelby tensor include logarithmic singularity at the origin (Mura 2013). In the case of the existence of an applied remote strain, $\boldsymbol{\epsilon}^{0}$, the total strain can be written as

$$
\boldsymbol{\epsilon} = \boldsymbol{\epsilon}^{0} + \boldsymbol{\epsilon}^{\mathrm{d}}.
\tag{8}
$$

Assuming linear theory of elasticity, the elastic strain $\mathbf{e}$ in the subdomain C is

$$
\mathbf{e} = \boldsymbol{\epsilon} - \boldsymbol{\epsilon}^{*} = \boldsymbol{\epsilon}^{0} + \boldsymbol{\epsilon}^{\mathrm{d}} - \boldsymbol{\epsilon}^{*}.
\tag{9}
$$

The Hooke's law can be written as

$$
\boldsymbol{\sigma} = \mathbf{C}\mathbf{e} = \mathbf{C}(\boldsymbol{\epsilon} - \boldsymbol{\epsilon}^{*}) = \mathbf{C}(\boldsymbol{\epsilon}^{0} + \boldsymbol{\epsilon}^{\mathrm{d}} - \boldsymbol{\epsilon}^{*}),
\tag{10}
$$

where $\mathbf{C}$ is the elastic moduli tensor. The equilibrium equation in the absence of body force is

$$\nabla \cdot \boldsymbol{\sigma} = \mathbf{0}. \tag{11}$$

By substituting Eqs. 10 in 11 we have

$$\nabla \cdot \mathbf{C}(\boldsymbol{\epsilon}) = \nabla \cdot \mathbf{C}(\boldsymbol{\epsilon}^*). \tag{12}$$

By writing strain field in the left-hand-side of the above equation in terms of displacement field and also by considering isotropic material properties, the following equation is obtained, the left-hand-side of which reminds us of the well-known Navier equation (Landau and Lifshitz 1959; del Castillo 2003):

$$\nabla^2 \mathbf{u} + \frac{\nabla(\nabla \cdot \mathbf{u})}{(1-2\nu)} = \frac{1}{\mu} \nabla \cdot (\mathbf{C}\boldsymbol{\epsilon}^*), \tag{13}$$

where $\mathbf{u}$ is the displacement vector. Eq. 13 in the cylindrical coordinate system includes the following components:

$$\begin{aligned}
&\frac{\partial^2 u_r}{\partial r^2} + \frac{1}{r}\frac{\partial u_r}{\partial r} - \frac{u_r}{r^2} \\
&\quad + \frac{1}{r^2}\frac{1-2\nu}{2-2\nu}\frac{\partial^2 u_r}{\partial \theta^2} + \frac{1}{r}\frac{1}{2-2\nu}\frac{\partial^2 u_\theta}{\partial r \partial \theta} - \frac{1}{r^2}\frac{3-4\nu}{2-2\nu}\frac{\partial u_\theta}{\partial \theta} \\
&\quad = \frac{\partial \epsilon^*_{rr}}{\partial r} + \frac{\nu}{1-\nu}\frac{\partial \epsilon^*_{\theta\theta}}{\partial r} \\
&\quad + \frac{\nu}{1-\nu}\frac{\partial \epsilon^*_{zz}}{\partial r} + \frac{1}{r}\frac{1-2\nu}{1-\nu}\frac{\partial \epsilon^*_{r\theta}}{\partial \theta} \\
&\quad + \frac{1-2\nu}{1-\nu}\frac{\epsilon^*_{rr}}{r} - \frac{1-2\nu}{1-\nu}\frac{\epsilon^*_{\theta\theta}}{r},
\end{aligned} \tag{14a}$$

$$\begin{aligned}
&\frac{\partial^2 u_\theta}{\partial r^2} + \frac{1}{r}\frac{\partial u_\theta}{\partial r} - \frac{u_\theta}{r^2} \\
&\quad + \frac{1}{r^2}\frac{2-2\nu}{1-2\nu}\frac{\partial^2 u_\theta}{\partial \theta^2} \\
&\quad + \frac{1}{r}\frac{1}{1-2\nu}\frac{\partial^2 u_r}{\partial r \partial \theta} + \frac{1}{r^2}\frac{3-4\nu}{1-2\nu}\frac{\partial u_r}{\partial \theta} \\
&\quad = 2\frac{\partial \epsilon^*_{r\theta}}{\partial r} + \frac{1}{r}\frac{2-2\nu}{1-2\nu}\frac{\partial \epsilon^*_{\theta\theta}}{\partial \theta} \\
&\quad + \frac{1}{r}\frac{2\nu}{1-2\nu}\frac{\partial \epsilon^*_{rr}}{\partial \theta} + \frac{1}{r}\frac{2\nu}{1-2\nu}\frac{\partial \epsilon^*_{zz}}{\partial \theta} + 4\frac{\epsilon^*_{r\theta}}{r},
\end{aligned} \tag{14b}$$

$$\begin{aligned}
&\frac{\partial^2 u_z}{\partial r^2} + \frac{1}{r^2}\frac{\partial^2 u_z}{\partial \theta^2} + \frac{1}{r}\frac{\partial u_z}{\partial r} \\
&\quad = 2\frac{\partial \epsilon^*_{rz}}{\partial r} + \frac{2}{r}\frac{\partial \epsilon^*_{\theta z}}{\partial \theta} + \frac{2}{r}\epsilon^*_{rz},
\end{aligned} \tag{14c}$$

which are the same as equations that were previously derived by Shokrolahi-Zadeh and Shodja (2008). Equations 14 are the governing equations to be solved for a given eigenstrain $\boldsymbol{\epsilon}^*$. We will consider that $\boldsymbol{\epsilon}^*$ has the following form in cylindrical coordinates:

$$\epsilon^*_{ij}(r,\theta) = \epsilon^*_{ij} r^n e^{\imath\eta\theta}. \tag{15}$$

The solution of Eqs. 14 corresponding to an $\epsilon^*_{ij}(r,\theta)$ in the form of Eq. 15, can be expressed as (Mura 2013)

$$u_i(r,\theta) = u_i r^n e^{\imath\eta\theta}. \tag{16}$$

For the case of axisymmetric eigenstrain, the solution should not depend on θ, therefore $\eta = 0$. By substituting $u_i(r,\theta)$ in the form of Eq. 16 in Eqs. 14 and setting the right-hand-side equal to zero, $n = \pm 1$ is obtained for the general solution to Eqs. 14 for the case of $\eta = 0$. Since inside the inclusion, the disturbance displacement should be finite and far away outside the inclusion, the disturbance displacement should approach to zero, it can be concluded that $n = 1$ is legitimate for inside the inclusion and $n = -1$ is legitimate for outside the inclusion. Therefore, the general solution for the homogeneous (denoted by superscript h below) part of Eqs. 14 is as follows:

$$u^h_r(r) = c_1 r, \tag{17}$$

$$u^h_\theta(r) = c_2 r, \tag{18}$$

$$u^h_z(r) = c_3, \tag{19}$$

for $r < R$, and

$$\begin{aligned}
u^h_r(r) &= \frac{c_4}{r}, \\
u^h_\theta(r) &= \frac{c_5}{r}, \\
u^h_z(r) &= c_6,
\end{aligned} \tag{20}$$

for $r > R$, where c_is ($i = 1, 2, \ldots, 6$) are constants to be determined from boundary conditions (Supplementary Eqs. S8 and S9). Since the disturbance displacement far away from the inclusion should approach to zero, we can conclude that $c_6 = 0$. The homogeneous solution is independent from the eigenstrain. For $r > R$, the eigenstrain and the right-hand-side of Eqs. 14 are identically equal to zero. For $r < R$ however, the eigenstrain is nonzero and non-uniform in general. For a general form of eigenstrain, obtaining the particular solution to the non-homogeneous Eqs. 14 can be troublesome. However, for the eigenstrain in the form of a polynomial with respect to r, the following expansion can be considered (15):

$$\boldsymbol{\epsilon}^*(r) = \sum_n \sum_{i,j=r,\theta} \epsilon^*_{ij}\, r^n\, \mathbf{e}_i\, \mathbf{e}_j, \tag{21}$$

where $\boldsymbol{\epsilon}^*(r)$ is also axisymmetric (corresponding to $\eta = 0$). In the context of linear elasticity, the disturbance strain corresponding to the eigenstrain, Eq. 21, can be obtained by superimposing the solutions for individual terms for each n. It can be seen that for an integer value of n, the following form satisfies Eqs. 14 for properly chosen constants, and thus can be used as a particular (denoted by superscript p below) solution to Eqs. 14:

$$\begin{aligned} u_r^p(r) &= k_1 r^{a_1} (\ln r)^{a_2}, \\ u_\theta^p(r) &= k_2 r^{a_3} (\ln r)^{a_4}, \\ u_z^p(r) &= k_3 r^{a_5} (\ln r)^{a_6}, \end{aligned} \tag{22}$$

where constants $a_1, a_2, \ldots, a_6$ and k_1, k_2, k_3 need to be selected for each n such that the governing Eqs. 14 and the boundary conditions are satisfied. The boundary conditions are based on continuity of displacements across the boundary of inclusion and matrix as well as continuity of traction stresses. These boundary conditions are given in Supplementary Eqs. S8 and S9. The rest of the procedure consisting of finding the particular solution and satisfying the boundary conditions in addition to an example showing the steps for deriving the components of Eshelby tensor for uniform eigenstrain field, are discussed in the SI. As the result, components of the Eshelby tensor as defined by Eq. 7 for $(\eta, n) = (0, 0)$ and for the rr component of the eigenstrain field are obtained as

$$\begin{aligned} D_{rrrr}^{\mathrm{C}(0,0)} &= \frac{3 - 4\nu + 2(1-2\nu)\ln(r/R)}{4(1-\nu)}, \\ D_{\theta\theta rr}^{\mathrm{C}(0,0)} &= \frac{1 + 2(1-2\nu)\ln(r/R)}{4(1-\nu)}, \\ D_{r\theta rr}^{\mathrm{C}(0,0)} &= D_{rzrr}^{\mathrm{C}(0,0)} = D_{\theta zrr}^{\mathrm{C}(0,0)} = D_{zzrr}^{\mathrm{C}(0,0)} = 0, \end{aligned} \tag{23}$$

$$\begin{aligned} D_{rrrr}^{\mathrm{M}(0,0)} &= -D_{\theta\theta rr}^{\mathrm{M}(0,0)} = -\frac{1}{4(1-\nu)}(R/r)^2, \\ D_{r\theta rr}^{\mathrm{M}(0,0)} &= D_{rzrr}^{\mathrm{M}(0,0)} = D_{\theta zrr}^{\mathrm{M}(0,0)} = D_{zzrr}^{\mathrm{M}(0,0)} = 0. \end{aligned} \tag{24}$$

Through a similar procedure, for other components ($\theta\theta, r\theta$, etc.) of the uniform eigenstrain field, components of the Eshelby tensor are derived and are presented in the SI. Strain and stress components can be readily obtained by substitution of the components of the Eshelby tensor in Eqs. (7 - 10).

2.1.4 Implementation of the Eshelby's inclusion for the cell problem

2.1.4.1 Contractility Having derived expressions for the Eshelby tensor, we are now ready to tackle the target cell problem. The numerical study in Supplementary Figs. 2 and 3 of the SI shows that anisotropy in elastic moduli has the same qualitative effect as anisotropic contractility. Therefore, here we assume only isotropic elastic moduli tensor for the cell layer, but either isotropic or anisotropic contractility. We derive the analytical solution for both isotropic and uniform anisotropic contractility. We will confirm our analytical solutions with numerical results later in the Finite Element Modeling section, where we will further address non-uniform contractility as well. As was also mentioned before, eigenstrain is a mathematical concept to model contractility in the material by $\epsilon^*(r,\theta,z) = \alpha_{ij}(r,\theta,z)\Delta T \delta_{ij}$ in which ΔT is the change in temperature and α_{ij} is coefficient of thermal expansion (with only nonzero components α_{rr}, $\alpha_{\theta\theta}$, and α_{zz}). For the uniform isotropic ($\alpha_{rr} = \alpha_{\theta\theta} = \alpha_{zz}$) contractility case, $\epsilon^*_{rr} = \epsilon^*_{\theta\theta} = \epsilon^*_{zz}$. Since we assume the cell problem is axisymmetric (i.e., independent of θ), $\eta = 0$ in Eq. 2. Moreover, for the uniform contractility/eigenstrain cases, $n = 0$ in Eq. 15 of the analytical solution. This means that we need components of the Eshelby tensor for $(\eta, n) = (0, 0)$ only (which have been derived and presented in the previous section of this paper as well as the SI).

2.1.4.2 Boundary conditions Cells are attached to the substrate via focal adhesions. Both in single cells and in multicellular aggregates, focal adhesions are not uniformly distributed. Focal-adhesion-associated proteins are reported to exist dominantly in periphery of a single cell and an aggregate (Stolarska and Rammohan 2017; Gallant et al. 2005; Girard and Nerem 1995; Kilian et al. 2010; Oakes et al. 2014). This suggests that the cell layer is tightly connected to the substrate around the edge. In our theoretical model, we consider the cell layer free on top and bottom surfaces, but it has displacement boundary conditions at the edge $r = R$. The challenge however is that, in the Eshelby problem, there exists a remote strain field applied to an infinite surrounding medium. This is not the case for the cell problem. In order to equalize the finite-medium cell problem with the infinite-medium Eshelby problem, and to figure out the equivalent far-field strains in the Eshelby problem, we suggest and follow the below algorithm:

1. Numerically model the cell layer with the applied eigenstrain and the desired displacement boundary conditions at the edge (as will be discussed in depth in the next section).
2. Read the resulting six values of stress components at the edge boundary.
3. Tune the applied far-field strains in the Eshelby problem so that the resulting analytical stresses at the edge of the inclusion are consistent with the stress values of numerical results at Step 2.

In this study, for the analytical solution, we consider a free cell layer (i.e., cells are not attached to the substrate below them), for which only one stress component at the edge, $\sigma_{\theta\theta}|_{r=R}$, is unknown and can be taken as an input from numerical results. We will later show that the behavior of the resulting stress field for a cell layer with free boundary condition and a cell layer that is fixed at the edge are qualitatively consistent.

2.2 Finite element modeling

2.2.1 2-D model

We use two-dimensional (2-D) finite-element models to validate our theoretical model for free single cell and aggregate layers with isotropic and uniform anisotropic cell layer properties (more realistic contractility and boundary conditions are studied in the next section using a 3-D model). For this purpose, 2-D models of circular cell layers with radii of 100 μm and 10 μm corresponding to a cell aggregate and a single cell respectively, are built in the commercial software Abaqus. The cell layer is modeled as a continuous elastic isotropic layer with Young's modulus of 40 kPa and Poisson's ratio of 0.49 (nearly incompressible). The properties for the cell layer are taken from Ref. (Goldblatt 2020). Standard plane stress quad element with mesh refinement at the center of the cell layer is used to discretize the model. A free boundary condition, i.e., the boundary of the cell layer can deform with no restriction, is considered consistent with the analytical solution. A pre-strain is introduced using a temperature drop of 1 K, in which case $\epsilon^*(r,\theta,z) = -\alpha_{ij}(r,\theta,z)\delta_{ij}$. In order to study the effect of anisotropic contractility, different anisotropy ratio $\kappa = \alpha_{\theta\theta}/\alpha_{rr}$ are considered consistent with the analytical solution. These values are tabulated in Table 1. Stress fields for a cell aggregate and a single cell layer for different anisotropy ratios are presented and compared with the analytical solution in Figs. 3 and 4.

Table 1 Anisotropy ratios used in the analytical and numerical analysis

κ	$\alpha_r(K^{-1})$	$\alpha_\theta(K^{-1})$	$\alpha_z(K^{-1})$
0.5	0.03	0.015	0.015
1	0.02	0.02	0.02
2	0.015	0.03	0.015
10	0.005	0.05	0.005

Note that all figures of this paper only plot σ_{rr} and $\sigma_{\theta\theta}$ components of stress. This is because other components are negligible, as illustrated in the Supplementary Fig. 1 of the SI for different boundary conditions as well as isotropic and anisotropic contractility.

2.2.2 3-D model

We use three-dimensional (3-D) finite-element model to study a more realistic contractility model for multi-cellular aggregates, based on experimental observations in Fig. 1a and (Goldblatt 2020), as well as more realistic boundary conditions. Based on these experimental observations, *non-uniform* contractility is suggested and further implemented and then compared with the results of isotropic and uniform contractility. Variation of contractility along the radius for all three contractility models are depicted in Fig. 5a. For *non-uniform* contractility, it is assumed that $\alpha_{rr} = \alpha_{\theta\theta} = \alpha_{zz}$ at the center, consistent with the observation that the fibers are not aligned in any specific direction at the center. However, $\alpha_{\theta\theta}$ increases radially with maximum value at the edge, consistent with the maximum fiber alignment in the θ direction at the edge. We will assume that the increase in $\alpha_{\theta\theta}$ from center to the edge is linear in r, with $\alpha_{\theta\theta}(r)|_{r=R}/\alpha_{\theta\theta}(r)|_{r=0} = 2$.

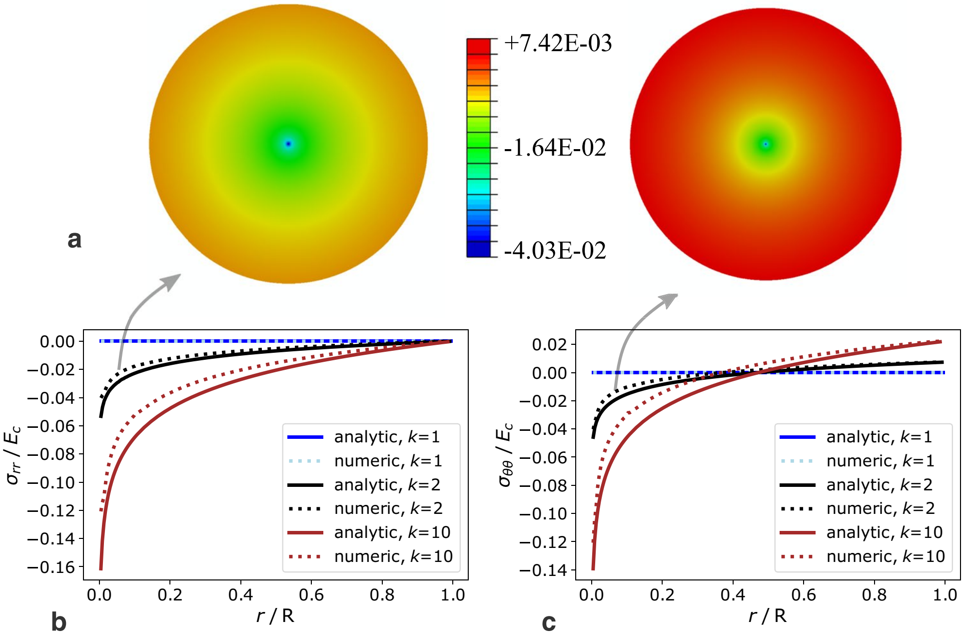

Fig. 3 **a** Heat maps of numerically predicted radial (left) and circumferential (right) stress fields inside a hypothetical 2-D free cell layer (aggregate) with uniform anisotropy for $\kappa = \alpha_{\theta\theta}/\alpha_{rr} = 2$. Predicted analytical and numerical radial **b** and circumferential **c** stresses for different anisotropy ratios $\kappa = 1, 2, 10$ inside a hypothetical 2-D free cell layer. In the numerical finite-element simulations, 40 kPa and 100 μm have been used for the Young's modulus (E_c) and radius of the cell layer (R) respectively

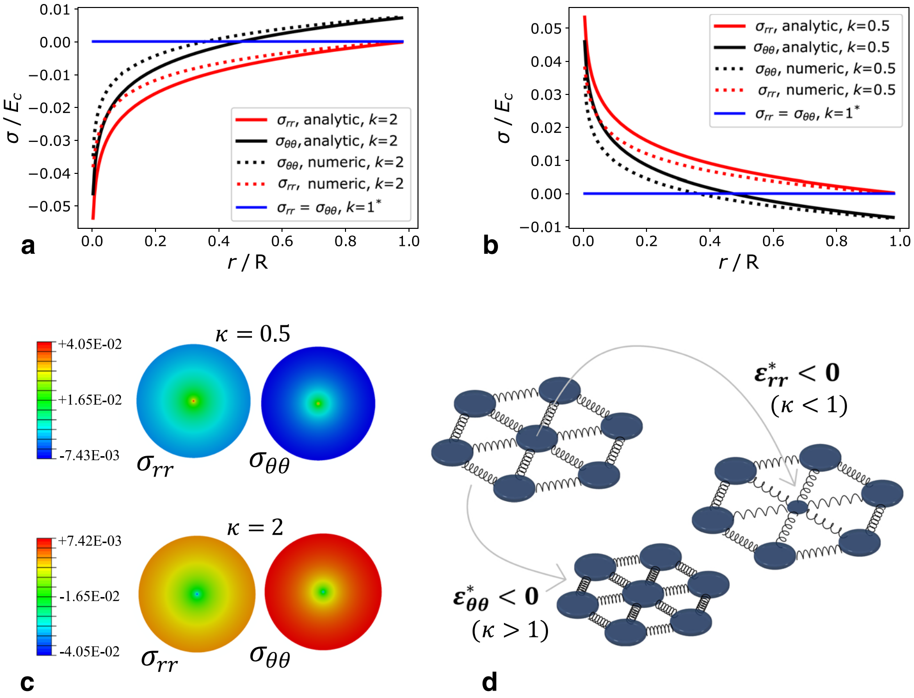

Fig. 4 **a**, **b** and **c** Results for a hypothetical 2-D free cell layer (single cell) with isotropic and uniform anisotropic contractility. In the numerical finite-element simulations, 40 kPa and 100 μm have been used for the Young's modulus (E_c) and radius of the cell layer (R), respectively. * Numeric and analytic are coinciding for $\kappa = 1$. **a** Predicted analytical and numerical radial and circumferential stresses for $\kappa = 1$ (isotropic) versus $\kappa = 2$ (circumferential fiber alignment). **b** Predicted analytical and numerical radial and circumferential stresses for $\kappa = 1$ (isotropic) versus $\kappa = 0.5$ (radial fiber alignment). **c** Heat maps of numerically predicted radial and circumferential stress field for $\kappa = 0.5$ (top) and $\kappa = 2$ (bottom). **d** A schematic representation of the behavior of the cell layer at the center showing compression for $\kappa > 1$ and tension for $\kappa < 1$

The value of this ratio will not qualitatively change the predicted stress field. Also, since most of the fiber alignment is observed in the θ direction, we will assume that $\alpha_{rr} = \alpha_{zz}$ remains constant along radius. To make a fair comparison between the three cases of isotropic contractility, uniform anisotropic contractility, and non-uniform anisotropic contractility, we have kept the overall contractility equal. For this purpose, α values are chosen so that the area under the contractility-radius curve, $\int_0^R (\alpha_{rr}(r) + \alpha_{\theta\theta}(r) + \alpha_{zz}(r))\mathrm{d}r$, is identical for all the three cases.

A 3-D finite-element model of a circular cell layer (radius 100 μm corresponding to the aggregate dimension) and substrate (radius 200 μm to serve as a planar semi-infinite substrate and avoid the edge effects) was then constructed. The thickness of the cell and substrate layers are 3.2 and 1 μm, respectively, consistent with previous works (Goldblatt 2020; He 2015). The cell layer and substrate layer were modeled as elastic isotropic materials with Young's moduli of 40 and 0.4 kPa, respectively [a softening effect caused by the adhesive bonding layer between the cell layer and the substrate is considered (Goldblatt 2020)]. Poisson's ratios of both the cell and substrate layers were considered as 0.49. The properties are all taken from Ref. (Goldblatt 2020). Similar to the previous case, a pre-strain is introduced using a temperature drop of 1 K. The model is then run for three material models of Fig. 5a: (i) isotropic contractility, (ii) uniform anisotropic contractility for $\kappa = 2$, and (iii) linear non-uniform anisotropic contractility. Each of the cases above is run for two different boundary conditions and the stress values are extracted at the bottom of the cell layer: (i) The periphery of the cell layer is attached to the substrate and the bottom surface of the substrate is fixed. The results are shown in Fig. 5b. (ii) The cell layer is uniformly attached to the substrate and the bottom surface of the substrate is fixed. The results are shown in Fig. 5c.

3 Results

3.1 Uniform anisotropy results in infeasible stress concentration

The results of analytical and numerical analysis for a free two-dimensional cell aggregate layer with a radius equal to 100 μm and different values of anisotropy ratio $\kappa = \alpha_{\theta\theta}/\alpha_{rr}$ are shown in Fig. 3. $\kappa = 1$ is equivalent to the case of

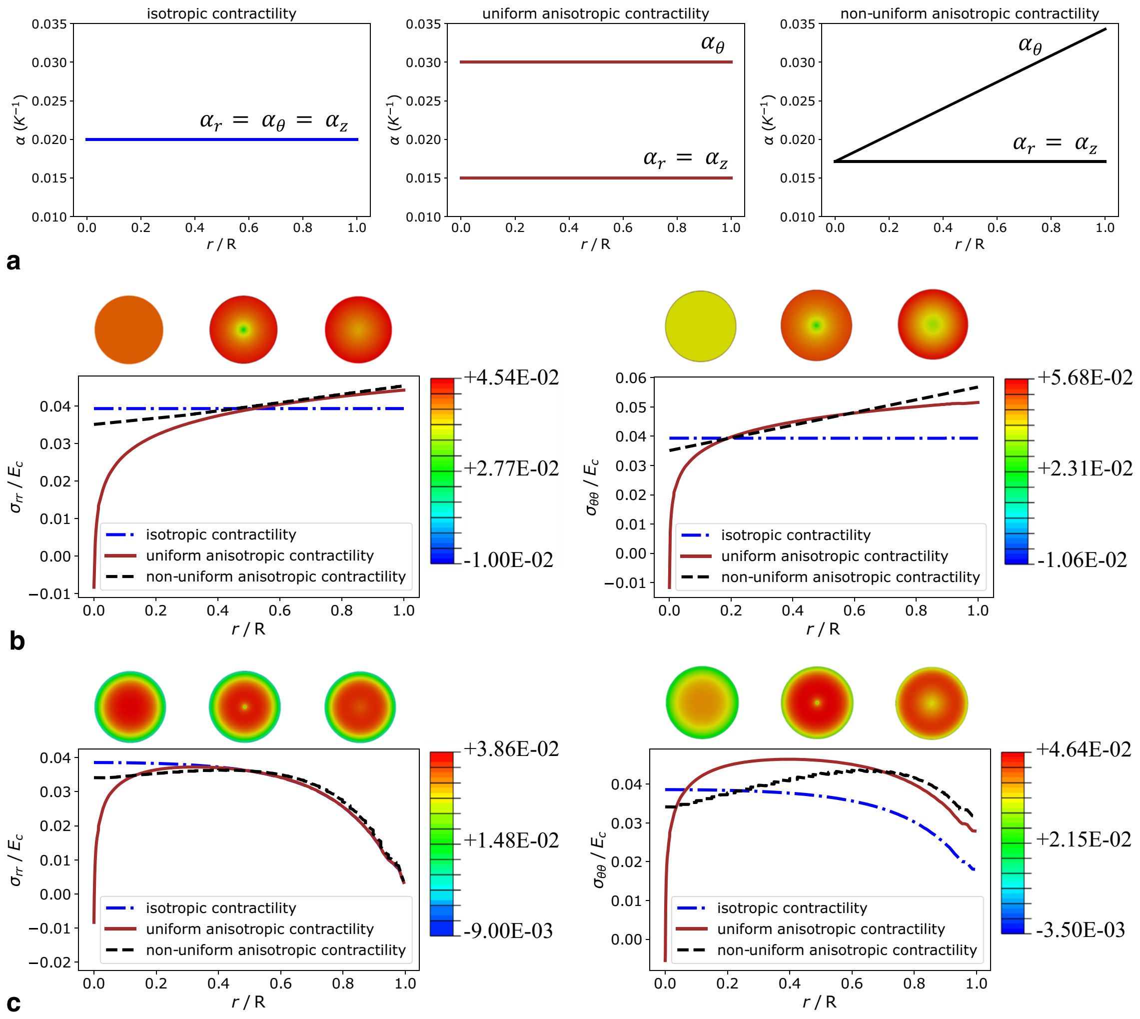

Fig. 5 **a** Representation of isotropic contractility, uniform anisotropic contractility and non-uniform anisotropic contractility models used in the 3-D finite-element analysis. **b**, **c** Predicted numerical results for a 3-D model of cell layer (aggregate) for realistic boundary conditions with contractility models shown in **a**. In the numerical finite-element simulations, 40 kPa and 100 μm have been used for the Young's modulus (E_c) and radius of the cell layer (R), respectively. **b** Radial (left) and circumferential (right) stress fields for a cell layer that is fixed at the periphery only (corresponding to the realistic case where focal adhesions are present mostly at the edge). **c** Radial (left) and circumferential (right) stress fields for a cell layer that is uniformly attached to the substrate

isotropic contractility ($\alpha_{rr} = \alpha_{\theta\theta}$). $\kappa = 2$ and $\kappa = 10$ are equivalent to the cases where fibers are aligned in the circumferential direction causing $\alpha_{\theta\theta} = 2\alpha_{rr}$ and $\alpha_{\theta\theta} = 10\alpha_{rr}$, respectively. As it is expected, the radial stress at $r = R$ for all κ values in both numerical and analytical results is zero. This is because the periphery of the disc is considered free (zero traction). The circumferential stress at $r = R$ is in general nonzero as $\sigma_{\theta\theta}$ is not a traction component. Also, we can see that for the isotropic case, $\kappa = 0$, both radial and circumferential stress components are zero as we expect for a freely contracting isotropic circular disk. This shows the results are verified against intuitive boundary conditions. In addition, a good agreement is observed between numerical and analytical results. It is seen that there is no radial and circumferential stress within the cell layer for isotropic contractility $\kappa = 1$. For the cases of $\kappa = 2$ and $\kappa = 10$, the radial compressive stress diminishes at the edge (due to free boundary condition) and increases moving radially toward the center of the aggregate. The values of circumferential stress are positive at the periphery of the cell layer and reduce as moving radially toward the center. An interesting observation is that a large radial and circumferential compressive stress concentration appears at the center of the cell layer for the case of the uniform anisotropic contractility with $\kappa = 2$ and $\kappa = 10$ (which does not exist for isotropic contractility). We will later suggest a simple disk-spring model and show that compression near the center happens as long as $\kappa > 1$, irrespective of its exact value. It is seen that the change in the stress sign occurs at a distance equal to around 40% of the cell radius from the center. In other words, cells within the interior parts of the aggregate (within the area $r \lesssim 0.4R$) experience both compressive radial and compressive circumferential stresses whereas cells outside this region experience a tensile circumferential stress and a compressive radial stress.

3.2 Effect of stress fiber alignment

Analytical and numerical results for isotropic as well as anisotropic contractility for a free 2-D single cell layer with a radius equal to 10 μm are presented in Fig. 4. As opposed to Fig. 3 which only includes $\kappa \geq 1$, here the results for $\kappa = 2$ and $\kappa = 0.5$ are presented and compared. κ less than one for single cell layer is inspired by earlier experiments reported in the literature reprinted in Fig. 1. Specifically, $\kappa = 0.5$ here is equivalent to the case that fibers are aligned in the radial direction causing $\alpha_{\theta\theta} = 0.5\alpha_{rr}$. A good agreement is observed between numerical and experimental results. Qualitatively consistent with the aggregate cell layer case, the results show no stress within the cell layer for $\kappa = 1$, and a compressive stress concentration at the center for $\kappa = 2$ (Fig. 4a, c). However, tensile stress concentration is observed for $\kappa = 0.5$ (Fig. 4b, c). In other words, when $\kappa > 1$, the stress concentration at the center of the cell is compressive whereas when $\kappa < 1$, the stress concentration at the center of the cell is tensile.

This result might not look intuitive at first glance. In order to help clarify this phenomenon, a schematic model of a system of disks and springs is shown in Fig. 4d to represent the center of the cell. The top left conformation of disk-spring system in Fig. 4d represents the initial unstressed condition. Also, the circumferential contraction is represented by a decrease in the periphery of the hexagonal disk-spring system, as shown in the bottom conformation in Fig. 4d for the extreme case of circumferential contraction and no radial contraction ($\kappa = \infty$). On the other hand, the radial contraction is represented by a decrease in the radius of the central disk, as shown in the right conformation in Fig. 4d for the extreme case of radial contraction and no circumferential contraction ($\kappa = 0$). Interestingly, this simple system suggests that for the case of $\kappa = 1$, there should be no stress induced in the system, which is consistent with the results of the cell system in Fig. 4a, b. Moreover, for $\kappa > 1$, the simple disk-spring system suggests compression near the center (shown with a reduction in the length of central springs), and for $\kappa < 1$ tension near the center (shown with an increase in central springs' length), all consistent with analytical and numerical results of Figs. 3, 4a, b for the cell system.

3.3 Extending to experimentally-based anisotropic contractility model with more realistic boundary conditions

In order to extend this research to more realistic boundary conditions and contractilities, a numerical study for a 3-D model of the cell aggregate is next performed for three cases of contractility: (i) isotropic, (ii) uniform anisotropic, and (iii) the proposed experimentally-based non-uniform anisotropic contractility. The results are shown in Fig. 5, with the values of contractility that are used for this analysis being reported in Fig. 5a. The radial and circumferential stress fields for a cell layer that is fixed at the periphery only (corresponding to the realistic case where focal adhesions are present mostly at the edge) are shown in Fig. 5b. It is seen that while the values of radial and circumferential stresses are different from those of free boundary condition (Fig. 3), the overall trends are the same. This emphasises the fact that the proposed simplified hypothetical model serves as a basis for more complex boundary conditions. The results show that both σ_{rr} and $\sigma_{\theta\theta}$ take positive values at the edge, with higher values for both uniform and non-uniform anisotropic contractility as compared to isotropic contractility. However, stresses drop moving along the radius toward the center for the cases of uniform and non-uniform anisotropic contractility. Eventually, in the central region, the stress values are much smaller for uniform anisotropic contractility (and to a less extent for non-uniform anisotropic contractility) as compared to isotropic contractility. Similar to the 2-D case with free boundary condition, compressive stress concentration is observed for the case of uniform anisotropic contractility in the central region of the cell. Interestingly, the more realistic non-uniform anisotropic contractility model (which is suggested based on the experimentally observed bio-markers) suppresses the large non-realistic stress concentration at the cell center. This is consistent with the results of Simon et al. who showed the necessity of radial variations in the cell layer material behavior, including cell contraction (Simon and Humphrey 2012).

Finally, note the difference in stress values between isotropic, non-uniform anisotropic, and uniform anisotropic contractility; e.g., 44% increase in $\sigma_{\theta\theta}$ at the edge for non-uniform anisotropic as compared to isotropic, and 31% for uniform anisotropic as compared to isotropic. While most available techniques (e.g., Traction Force Microscopy) assume isotropic material property to predict the stress in the cell layer from measured displacement fields, here we show that neglecting anisotropy can lead to considerable errors in the stress predictions. Our results show the importance of considering more realistic properties for evaluating the stress fields within the cell layer.

Figure 5c shows stress values for a cell layer that is uniformly attached to a substrate. There are similarities and differences for uniformly-attached boundary condition as compared to the earlier periphery-fixed boundary condition. Similar to the periphery-fixed boundary condition, a stress concentration for both σ_{rr} and $\sigma_{\theta\theta}$ is observed at the center of the cell layer for uniform anisotropic contractility, but not for non-uniform anisotropic contractility. Also, due to larger values and/or changes in $\alpha_{\theta\theta}$ as compared to α_{rr}, (Fig. 5a), the effect of anisotropic contractility model is more pronounced for $\sigma_{\theta\theta}$ as compared to σ_{rr} (left versus right in Fig. 5c).

Dissimilar to the periphery-fixed boundary condition, σ_{rr} and $\sigma_{\theta\theta}$ increase from edge moving toward the center in isotropic, uniform anisotropic and non-uniform anisotropic contractility cases. This increase in the stress values which occurs mostly at the edge is due to the traction that is applied by the substrate to the cell layer at the interface (Goldblatt 2020). Moving further toward the center, σ_{rr} and $\sigma_{\theta\theta}$ show a plateau and reach their maximum values at the cell center for the isotropic contractility model. For the uniform anisotropic contractility model, σ_{rr} and $\sigma_{\theta\theta}$ drop sharply at the vicinity of the center. In the non-uniform anisotropic contractility model, σ_{rr} and $\sigma_{\theta\theta}$ show a gradual decrease after the initial increase. In other words, a larger portion of the cell layer will experience the stress drop in the case of non-uniform anisotropic contractility, whereas a smaller portion of the cell will feel a much more drastic stress drop in the uniform anisotropic contractility model.

By comparing Fig. 5b, c, we can see that the effect of anisotropic contractility model is more pronounced for the periphery-fixed boundary condition as compared to the case that the cell layer is uniformly attached to the substrate, e.g., for uniform anisotropy, the stress curve changes from the blue horizontal line to the nonlinear red curve with the periphery-fixed boundary condition in Fig. 5b, however with uniform attachment in Fig. 5c, apart from the center, the behavior does not change drastically. This higher sensitivity of the predicted stress field to anisotropic contractility for the periphery-fixed boundary condition is due to the ease of deformation in the loosely attached interior cells. Note that the periphery-fixed and uniform attachment of the cell layer to the substrate are two extreme cases and the realistic case is something in between.

Finally, we have previously shown that multiple stress sensitive biological measures (e.g., α-smooth-muscle-actin-rich stress fibers), indicate low stress in the center of multicellular aggregates and high circumferential stress at the periphery (Goldblatt 2020). This trend is in agreement with the stress field that resulted from the realistic non-uniform anisotropic contractility model, Fig. 5b, c, while the stress field predicted by the isotropic contractility model shows an inconsistent trend (Fig. 5b) or even an opposite trend (Fig. 5c) to the observed stress-related biological measures.

4 Discussion

In this study we model the circularly shaped aggregates that are cultured to confluence or post-confluence levels, as well as circularly shaped single cells, as a continuous thin cylindrical layer. We assume that the cells are not highly motile, so the small-strain theory of elasticity is valid for the model. Also, we assume linear elastic behavior, which is a simplification of the viscoelastic model and has been widely used to theoretically express the stress-strain relationship in living cells (Nelson 2005; He 2015; Tambe 2013). One of the limitations of this model is that the time factor is neglected. Also, the mechanical behaviors of cells are complex and can change due to temperature and other environmental factors which are all topics of interest for future studies. In conclusion, in this work, using a combined analytical and computational approach we show that anisotropy has a major impact on the estimated stress field within living cells. Our results show: (i) The stress fields obtained for the non-uniform anisotropic contractility model are more consistent with experimental biomarkers as compared to isotropic contractility assumption (Goldblatt 2020; Cirka 2016). (ii) Analytical and computational results are in good agreement and show an unfeasible stress concentration at the center of the cell layer for uniform anisotropy model. The occurrence of stress concentration may explain the scarcity of fiber alignment at the center of both circular single cells or multi-cellular aggregates that is observed in experimental data. (iii) The stress singularity at the center diminishes for the realistic non-uniform experimentally-based contractility model. Although implemented in this work for circularly shaped aggregates and cells, the theory developed here is general and can be applied to other geometries and applications that involve anisotropy.

Supplementary information The online version contains supplementary material available at (https://doi.org/10.1007/s10237-022-01595-0).

Acknowledgements This work was funded in part by grants from the National Science Foundation (CMMI 1761432), the National Institutes of Health (2R15HL087257-02A1), and a Worcester Polytechnic Institute/University of Massachusetts Medical School Seed Grant. HAC, NR, and KLB designed the problem. HAC developed the analytical framework. HAC performed the numerical analysis. HAC, NR, and KLB interpreted the results. HAC wrote the manuscript. HAC, KLB, and NR revised the manuscript. Heather AC, and ZE Goldblatt are acknowledged for providing permission to use their results in Fig. 1a, b. Sina Askarinejad is acknowledged for providing insight on numerical modeling. The authors declare no competing financial interests. All the data that support the findings within this study can be found in Supplementary Information or are available from the corresponding author upon reasonable request.

Data availability The data that support the findings within this study can be found in supplementary materials or are available from the corresponding author upon reasonable request.

Declarations

Conflict of interest There are no conflicts of interest to declare.

References

Albert PJ, Schwarz US (2014) Dynamics of cell shape and forces on micropatterned substrates predicted by a cellular Potts model. Biophys J 106:2340

Allen S, Farris R (1990) Complications of cylindrical anisotropy on the properties of fibres. Polymer 31:1467

Aragona M et al (2013) A mechanical checkpoint controls multicellular growth through YAP/TAZ regulation by actin-processing factors. Cell 154:1047

Braeu FA, Aydin RC, Cyron CJ (2019) Anisotropic stiffness and tensional homeostasis induce a natural anisotropy of volumetric growth and remodeling in soft biological tissues. Biomech Model Mechanobiol 18:327

Cabezas MD, Meckes B, Mirkin CA, Mrksich M (2019) Subcellular control over focal adhesion anisotropy, independent of cell morphology, dictates stem cell fate. ACS Nano 13:11144

Cirka HA (2016) Mechanical regulation of apoptosis and calcification within valvular interstitial cells, Ph.D. thesis, Worcester Polytechnic Institute

Crouch AS, Miller D, Luebke KJ, Hu W (2009) Correlation of anisotropic cell behaviors with topographic aspect ratio. Biomaterials 30:1560

del Castillo GFT (2003) 3-D spinors, spin-weighted functions and their applications, vol. 32, Springer Science & Business Media

Discher DE, Mooney DJ, Zandstra PW (2009) Growth factors, matrices, and forces combine and control stem cells. Science 324:1673

Dupont S et al (2011) Role of YAP/TAZ in mechanotransduction. Nature 474:179

Efremov YM et al (2019) Anisotropy vs isotropy in living cell indentation with AFM. Sci Rep 9:1

Eshelby JD (1957) The determination of the elastic field of an ellipsoidal inclusion, and related problems. Proc R Soc Lond Series A Math Phys Sci 241:376

Farhadifar R, Röper J-C, Aigouy B, Eaton S, Jülicher F (2007) How much does the cell boundary contract in a monolayered cell sheet? Curr Biol 17:2095

Feng Y, Lee C-H, Sun L, Ji S, Zhao X (2017) Characterizing white matter tissue in large strain via asymmetric indentation and inverse finite element modeling. J Mech Behav Biomed Mater 65:490

Fouchard J, Mitrossilis D, Asnacios A (2011) Acto-myosin based response to stiffness and rigidity sensing. Cell Adh Migr 5:16

Gallant ND, Michael KE, García AJ (2005) Cell adhesion strengthening: contributions of adhesive area, integrin binding, and focal adhesion assembly. Mol Biol Cell 16:4329

Girard PR, Nerem RM (1995) Shear stress modulates endothelial cell morphology and F-actin organization through the regulation of focal adhesion-associated proteins. J Cell Physiol 163:179

Goldblatt ZE et al (2020) Heterogeneity profoundly alters emergent stress fields in constrained multicellular systems. Biophys J 118:15

Graner F, Glazier JA (1992) Simulation of biological cell sorting using a two-dimensional extended Potts model. Phys Rev Lett 69:2013

Grütter MG (2000) Caspases: key players in programmed cell death. Curr Opin Struct Biol 10:649

Gupta M et al (2015) Adaptive rheology and ordering of cell cytoskeleton govern matrix rigidity sensing. Nat Commun 6:1

Gupta SK, Li Y, Guo M (2019) Anisotropic mechanics and dynamics of a living mammalian cytoplasm. Soft Matter 15:190

Hazeltine LB et al (2012) Effects of substrate mechanics on contractility of cardiomyocytes generated from human pluripotent stem cells. Int J Cell Biol. https://doi.org/10.1155/2012/508294

He S et al (2015) Dissecting collective cell behavior in polarization and alignment on micropatterned substrates. Biophys J 109:489

Hemp W (1966) Foundations of Solid Mechanics. Fung YC. Prentice-Hall, New Jersey. 1965. 525 pp. Diagrams.£ 5., Aeronaut J, 70: 453

Honda H, Eguchi G (1980) How much does the cell boundary contract in a monolayered cell sheet? J Theor Biol 84:575

Hu S et al (2003) Intracellular stress tomography reveals stress focusing and structural anisotropy in cytoskeleton of living cells. Am J Physiol Cell Physiol 285:C1082

Hu S et al (2004) Mechanical anisotropy of adherent cells probed by a three-dimensional magnetic twisting device. Am J Physiol Cell Physiol 287:C1184

Huang Y et al (2019) Traction force microscopy with optimized regularization and automated Bayesian parameter selection for comparing cells. Sci Rep 9:1

Hur SS, Zhao Y, Li Y-S, Botvinick E, Chien S (2009) Live cells exert 3-dimensional traction forces on their substrata. Cell Mol Bioeng 2:425

Ingber D (1991) Integrins as mechanochemical transducers. Curr Opin Cell Biol 3:841

Kilian KA, Bugarija B, Lahn BT, Mrksich M (2010) Geometric cues for directing the differentiation of mesenchymal stem cells. Proc Natl Acad Sci 107:4872

Landau LD, Lifshitz EM (1959) Course of Theoretical Physics Vol 7: Theory and Elasticity, Pergamon press

Li B, Li F, Puskar KM, Wang JH (2009) Spatial patterning of cell proliferation and differentiation depends on mechanical stress magnitude. J Biomech 42:1622

Lim C, Zhou E, Quek S (2006) Mechanical models for living cells-a review. J Biomech 39:195

Liu C, He S, Li X, Huo B, Ji B (2016) Mechanics of cell mechanosensing on patterned substrate. J Appl Mech 83:051014

Lo C-M, Wang H-B, Dembo M, Wang Y-L (2000) Cell movement is guided by the rigidity of the substrate. Biophys J 79:144

Lu Y, Shi J, Nie G, Zhong Z (2016) An elasticity solution for transversely isotropic, functionally graded circular plates. Mech Adv Mater Struct 23:451

Mura T (2013) Micromechanics of defects in solids, Springer Science & Business Media

Mura T, Shodja H, Hirose Y (1996) Inclusion problems. Appl Mech Rev 41:15

Nelson CM et al (2005) Emergent patterns of growth controlled by multicellular form and mechanics. Proc Natl Acad Sci 102:11594

Ng MR, Besser A, Danuser G, Brugge JS (2012) Substrate stiffness regulates cadherin-dependent collective migration through myosin-II contractility. J Cell Biol 199:545

Oakes PW, Banerjee S, Marchetti MC, Gardel ML (2014) Geometry regulates traction stresses in adherent cells. Biophys J 107:825

Olson MF, Sahai E (2009) The actin cytoskeleton in cancer cell motility. Clin Exp Metas 26:273

Oral A, Anlas G (2005) Effects of radially varying moduli on stress distribution of nonhomogeneous anisotropic cylindrical bodies. Int J Solids Struct 42:5568

Peeters EA et al (2004) Anisotropic, three-dimensional deformation of single attached cells under compression. Ann Biomed Eng 32:1443

Sadd MH (2009) Elasticity: theory, applications, and numerics, Academic Press

Schaumann EN, Staddon MF, Gardel ML, Banerjee S (2018) Force localization modes in dynamic epithelial colonies. Mol Biol Cell 29:2835

Shodja H, Rad I, Soheilifard R (2003) Interacting cracks and ellipsoidal inhomogeneities by the equivalent inclusion method. J Mech Phys Solids 51:945

Shokrolahi-Zadeh B, Shodja H (2008) Spectral equivalent inclusion method: anisotropic cylindrical multi-inhomogeneities. J Mech Phys Solids 56:3565

Simon D, Humphrey J (2012) On a class of admissible constitutive behaviors in free-floating engineered tissues. Int J Non-Linear Mech 47:173

Smith PG, Deng L, Fredberg JJ, Maksym GN (2003) Mechanical strain increases cell stiffness through cytoskeletal filament reorganization. Am J Physiol Lung Cell Mol Physiol 285:L456

Stolarska MA, Rammohan AR (2017) Center or periphery? Modeling the effects of focal adhesion placement during cell spreading. PloS One 12:e0171430

Tambe DT et al (2011) Collective cell guidance by cooperative intercellular forces. Nat Mater 10:469

Tambe DT et al (2013) Monolayer stress microscopy: limitations, artifacts, and accuracy of recovered intercellular stresses. PLoS ONE 8:e55172

Tee YH et al (2015) Cellular chirality arising from the self-organization of the actin cytoskeleton. Nat Cell Biol 17:445

Ting T (1996) Pressuring, shearing, torsion and extension of a circular tube or bar of cylindrically anisotropic material. Proc R Soc Lond Series A Math Phys Eng Sci 452:2397

Trepat X et al (2009) Physical forces during collective cell migration. Nat Phys 5:426

Vogel V, Sheetz M (2006) A mechanical checkpoint controls multicellular growth through YAP/TAZ regulation by actin-processing factors. Local Force Geom Sens Regul Cell Funct Nat Rev Mol Cell Biol 7:265

Wan LQ et al (2010) Geometric control of human stem cell morphology and differentiation. Integr Biol 2:346

Wei F et al (2020) Stress fiber anisotropy contributes to force-mode dependent chromatin stretching and gene upregulation in living cells. Nat Commun 11:1

Wilson J, Baek S, Humphrey J (2013) Parametric study of effects of collagen turnover on the natural history of abdominal aortic aneurysms. Proc R Soc A Math Phys Eng Sci 469:20120556

Yin L, Elliott DM (2004) A biphasic and transversely isotropic mechanical model for tendon: application to mouse tail fascicles in uniaxial tension. J Biomech 37:907

Yu H, Sanday S, Chang C (1994) Elastic inclusions and inhomogeneities in transversely isotropic solids. Proc R Soc London Series A Math Phys Sci 444:239